Discovery of Interstellar *trans*-cyanovinylacetylene (HC≡CCH=CHC≡N) and vinylcyanoacetylene (H₂C=CHC₃N) in GOTHAM Observations of TMC-1

Kin Long Kelvin Lee[1] ⬝, Ryan A. Loomis[2] ⬝, Andrew M. Burkhardt[3] ⬝, Ilsa R. Cooke[4] ⬝, Ci Xue[5] ⬝, Mark A. Siebert[6] ⬝, Christopher N. Shingledecker[7] ⬝, Anthony Remijan[2] ⬝, Steven B. Charnley[8], Michael C. McCarthy[3] ⬝, and Brett A. McGuire[1,2,3] ⬝

[1] Department of Chemistry, Massachusetts Institute of Technology, Cambridge, MA 02139, USA; kelvlee@mit.edu, brettmc@mit.edu
[2] National Radio Astronomy Observatory, Charlottesville, VA 22903, USA
[3] Center for Astrophysics | Harvard & Smithsonian, Cambridge, MA 02138, USA
[4] Univ Rennes, CNRS, IPR (Institut de Physique de Rennes) - UMR 6251, F-35000 Rennes, France
[5] Department of Chemistry, University of Virginia, Charlottesville, VA 22904, USA
[6] Department of Astronomy, University of Virginia, Charlottesville, VA 22904, USA
[7] Benedictine College, Atchison, KS 66002, USA
[8] Astrochemistry Laboratory and the Goddard Center for Astrobiology, NASA Goddard Space Flight Center, Greenbelt, MD 20771, USA

Abstract

We report the discovery of two unsaturated organic species, *trans*-(E)-cyanovinylacetylene and vinylcyanoacetylene, using the second data release of the GOTHAM deep survey toward TMC-1 with the 100 m Green Bank Telescope. For both detections, we performed velocity stacking and matched filter analyses using Markov Chain Monte Carlo simulations, and for *trans*-(E)-cyanovinylacetylene, three rotational lines were observed at low signal-to-noise ($\sim 3\sigma$). From this analysis, we derive column densities of 2×10^{11} and $3 \times 10^{11}\,\mathrm{cm}^{-2}$ for vinylcyanoacetylene and *trans*-(E)-cyanovinylacetylene, respectively, and an upper limit of $< 2 \times 10^{11}\,\mathrm{cm}^{-2}$ for *trans*-(Z)-cyanovinylacetylene. Comparisons with G3//B3LYP semiempirical thermochemical calculations indicate abundances of the [H₃C₅N] isomers are not consistent with their thermodynamic stability, and instead their abundances are mainly driven by dynamics. We provide a discussion on how these species may be formed in TMC-1, with reference to related molecules like vinyl cyanide (CH₂=CHC≡N). As part of this discussion, we performed the same analysis for ethyl cyanide (CH₃CH₂C≡N), the hydrogenation product of CH₂=CHC≡N. This analysis provides evidence—at 4.2σ significance—of an upper limit to the column density of $< 4 \times 10^{11}\,\mathrm{cm}^{-2}$; an order of magnitude lower than previous upper limits toward this source.

1. Introduction

Radio observations of the Taurus Molecular Cloud (TMC) complex, particularly toward the prestellar cloud core TMC-1, have revealed a plethora of molecules ranging from the cyanopolyynes (HC$_n$N, for odd values of n), to free radicals (e.g., *l*-C₃H by Thaddeus et al. 1985), to carbenes (e.g., H₂C₆ by Langer et al. 1997), to ions (e.g., C₈H⁻ by Brünken et al. 2007). More recently, the discovery of benzonitrile (*c*-C₆H₅CN) by McGuire et al. (2018) has added an aromatic ring—noteworthy for its exceptional thermodynamic and chemical stability, and a key building block in biological systems and the formation of soot and interstellar dust—to this already rich inventory. Chemical models, however, currently do not have sufficiently efficient pathways to reproduce the abundance of these aromatic molecules, in part due to the lack of observational constraints on potential carbon-chain precursors (Burkhardt et al. 2021). Unlike the well-studied cyanopolyyne family, many of the partially saturated carbon-chains have never been detected and thus large unknowns for these models. As such, in order to determine the formation of even the simplest aromatics, robust abundance measurements of partially saturated species must be obtained. Understanding how molecules like benzonitrile may be formed, processed, and transported in the interstellar medium—in particular in cold, dark environments like TMC-1—has significant implications in the chemical evolution of these environments.

Our large-scale observing campaign with the 100 m Green Bank Telescope, GOTHAM (GBT Observations of TMC-1: Hunting for Aromatic Molecules), seeks to determine the chemical inventory of TMC-1 at an unprecedented level by performing a wide band spectral line survey at centimeter wavelengths at high uniform sensitivity (target 2 mK rms across the whole spectrum) and high resolution (0.05 km s⁻¹). As part of the first data release, molecules of considerable complexity were reported for the first time, including 1- and 2-cyanonaphthalene (C₁₀H₇CN) (McGuire et al. 2020b), *c*-C₅H₅CN (McCarthy et al. 2020b), HC₁₁N (Loomis et al. 2020), and HC₄NC (Xue et al. 2020). Many of these detections greatly benefited from combining signal processing techniques with Bayesian modeling, which enables identification of molecules in sparse line spectra even when no individual features are present above the noise. Furthermore, statistically robust derivations of parameters such as column density and excitation temperature can be determined using this treatment. For an overview of this method and its uses, the reader is referred to McGuire et al. (2020a).

In this paper, we examine evidence in the second data release of GOTHAM for three isomers in the H₃C₅N family: vinylcyanoacetylene (H₂C=CHC₃N, VCA), and the (E) and (Z) isomers of *trans*-cyanovinylacetylene (HC≡CCH=CHC≡N, CVA), as shown in Figure 1. They are extended variants of vinyl cyanide (CH₂CHCN), an unsaturated nitrile-bearing molecule that was

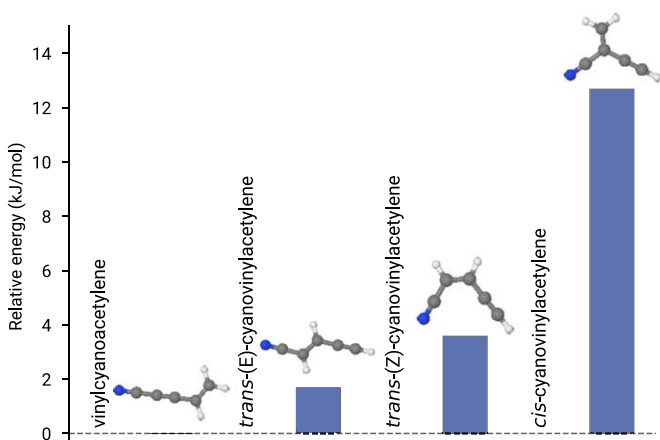**Figure 1.** G3//B3LYP energetics of the [H$_3$C$_5$N] structures of interest at 0 K, given relative to the lowest energy form, vinylcyanoacetylene.

first detected in this source by Matthews & Sears (1983). Given questions still persist as to how small branched hydrocarbon chains form in TMC-1 despite their structural simplicity (Vigren et al. 2009), simultaneous analysis of multiple isomers may provide insight into the operative formation pathways there. Of particular interest for this isomeric family is the possible connection with aromatic N-heterocycles such as pyridine, c-C$_5$H$_5$N, which might be formed by subsequent hydrogenation of one or more of the these isomers followed by ring closure.

2. Observations

Observations with the 100 m Green Bank Telescope (GBT) were carried out for the GOTHAM project, which has been detailed in a series of publications. Briefly, this work uses the second data release (henceforth referred to as DR2) of GOTHAM, which are observations targeting the well-known TMC-1 cyano-polyyne peak (CP) centered at $\alpha_{\rm J2000} = 04^{\rm h}41^{\rm m}42\overset{s}{.}5$, $\delta = +25°41'$ $26\overset{''}{.}8$ (McGuire et al. 2020a). As of DR2, our spectra cover the GBT X, K, and Ka bands from 7.906 to 33.527 GHz (25.6 GHz bandwidth) with continuous coverage between 22 and 33.5 GHz, at a uniform frequency resolution of 1.4 kHz (0.05–0.01 km s^{-1} in velocity) and an rms noise of ∼2–20 mK across the spectrum, with the rms increasing toward higher frequency due to limited integration time. Uncertainty due to flux calibration is expected to be ∼20%, based on complementary Very Large Array observations of the flux-calibrator source J0530 + 1331 (McGuire et al. 2020a).

3. Computational Methods

3.1. Quantum Chemistry

Calculations of the permanent electric dipole moment and relative energetics were performed using the Gaussian 16 suite of electronic structure programs (Frisch et al. 2016). For dipole moments, geometries were first optimized at the ωB97X-D/6-31+G(d) level of theory, and the one-electron properties calculated at the same level—based on our earlier benchmarking, this combination produces dipole moments with uncertainties on the order of ± 0.5 D and systematically overpredicts vibrationally averaged values by 0.1 D (Lee & McCarthy 2020). In terms of thermochemistry, we used the B3LYP variant of the G3 semiempirical model chemistry (Baboul et al. 1999), which has been shown to be a computationally cost-effective method

of obtaining near-chemically accurate energetics (∼120 K) (Simmie & Somers 2015).

3.2. MCMC Modeling

Details of the Markov Chain Monte Carlo (MCMC) simulations are described in depth by Loomis et al. (2020), and we only briefly discuss the relevant aspects here. The objective of these simulations is to properly model the physical parameters of molecules in TMC-1 where maximum likelihood methods generally fail due to high covariance and dimensionality. The model used in our study assumes a Gaussian shape for the spatial distribution of TMC-1, with parameters for the size of the source (SS), radial velocity ($v_{\rm LSRK}$), column density ($N_{\rm col}$), excitation temperature ($T_{\rm ex}$), and spectral linewidth (dv). Based on recent observations performed with the 45 m telescope at Nobeyama Radio Observatory (Dobashi et al. 2018, 2019; Soma et al. 2018), as well as our data (Loomis et al. 2020), emission from molecules in TMC-1 toward the cyanopolyyne peak display at least four individual velocity components, which are subsequently represented by independent source size, radial velocity, and column density parameters; in total, our model comprises 14 fitting parameters.

Line profile simulations were performed using MOLSIM (Lee & McGuire 2020). The MCMC simulations used wrapper functions in MOLSIM to ARVIZ (Kumar et al. 2019) and EMCEE (Foreman-Mackey et al. 2013); the former for analyzing the results of sampling, and the latter implements an affine-invariant MCMC sampler. As prior parameters, we used the marginalized posterior from modeling HC$_9$N chosen on the basis of chemical similarity. The prior distributions approximated as normal (i.e., $p(\theta) \sim N(\mu_\theta, \sigma_\theta)$ for parameter θ) with modifications to the variance σ_θ as to avoid overly constrictive/ influential priors. The MCMC analysis was performed first for *trans*-(E)-CVA, which produced the strongest response out of the molecules reported here. Convergence of the MCMC was confirmed using standard diagnostics such as the Gelman & Rubin (1992) $\hat{R}$ statistic, and by visually inspecting the posterior traces. The resulting posterior for *trans*-(E)-CVA was subsequently used as prior distributions for VCA and *trans*-(Z)-CVA, albeit with the source sizes constrained to the mean values of *trans*-(E)-CVA due to poorly convergent sampling. The results reported here are relatively insensitive to the choice of prior; comparison between benzonitrile and *trans*-(E)-CVA do not qualitatively change the statistics derived from the converged posteriors.

3.3. Velocity Stacking and Matched Filter Analysis

With the model posterior at hand, we can corroborate our simulations with the observed data through a combined velocity stack and matched filter analysis (Loomis et al. 2018, 2020). Briefly, the former involves a noise-weighted composite spectrum by stacking the observed spectra—in velocity space—using known molecular transition frequencies, and the latter performs a velocity stack of the spectral simulation based on the fitted parameters, and cross-correlated with the observational velocity stack. The advantage of this approach is the ability to derive statistical significance of a detection based on the impulse response in the cross-correlation: the significance, σ, directly quantifies how well our model reproduces the observed data in velocity space, even in lieu of individual observed transitions. Throughout the

Table 1
Theoretical Equilibrium Dipole Moments for the Molecules of Interest

	μ_a (Debye)	μ_b (Debye)
VCA	5.3	0.3
trans-(E)-CVA	4.2	0.6
trans-(Z)-CVA	2.7	2.8
cis-CVA	3.2	2.5

Note. Values are calculated at the ωB97X-D/6-31+G(d) level of theory, which have a nominal ± 0.5 D uncertainty (see Section 3.1).

GOTHAM studies, we have adopted a $\geqslant 5\sigma$ heuristic for what constitutes a molecular detection as determined by $HC_{11}N$ (Loomis et al. 2020).

4. Results and Discussion

4.1. Spectroscopy and Relative Energetics

Figure 1 shows the relative energetics of the four molecules under investigation, along with their equilibrium structures. The two lowest energy forms of $[H_3C_5N]$ are near-prolate tops, while the two higher energy forms are closer to the oblate limit. The highest energy form in our study, *cis*-cyanovinylacetylene, has not yet been experimentally observed whereas the remaining three isomers have been studied extensively in the laboratory (Halter et al. 2001; Thorwirth et al. 2004), and most recently observed in a discharge mixture of benzene and N_2 (McCarthy et al. 2020a). We have also omitted the linear chain form, CH_3C_4N, which is likely to be unstable by analogy to the cyanopolyynes.

Catalogs of rotational transitions were generated using the SPCAT program (Pickett 1991) based on spectroscopic parameters—including nitrogen-hyperfine splitting—reported in the cited publications. In all cases, our electronic structure calculations suggest sizable dipole moments along *a*- and *b*-inertial axes (Table 1) with the total dipole moment around $\sim$5 D; typical for $-C \equiv N$ bearing molecules. For the two molecules closer to the oblate limit, the total dipole moment is divided roughly equally between the *a*- and *b*-axes. Given that $I \propto \mu^2$, this means that on an individual line basis, the near-oblate isomers require an order of 2–3 times more sensitivity for detection compared to their near-prolate counterparts.

4.2. GOTHAM Observations

Based on the energetics shown in Figure 1, we attempted to search for individual transitions arising from the lower energy isomers. Upon inspection, the lowest energy isomer, VCA, does not exhibit any obvious features in our spectra. For the next isomer in energy, *trans*-(E)-CVA, Figure 2 shows three spectral windows centered at frequencies that correspond to two $K = 0$ and one $K = 1$ transitions. These windows hint at individual spectral features within our data, albeit at low significance.

4.3. Velocity Stack and Matched Filter Analysis

From our observations, only *trans*-(E)-CVA exhibits tentative individual spectral features—whereas conventional methods of analysis (i.e., least-squares fits) may be limited to deriving upper limits to column densities, here we can combine
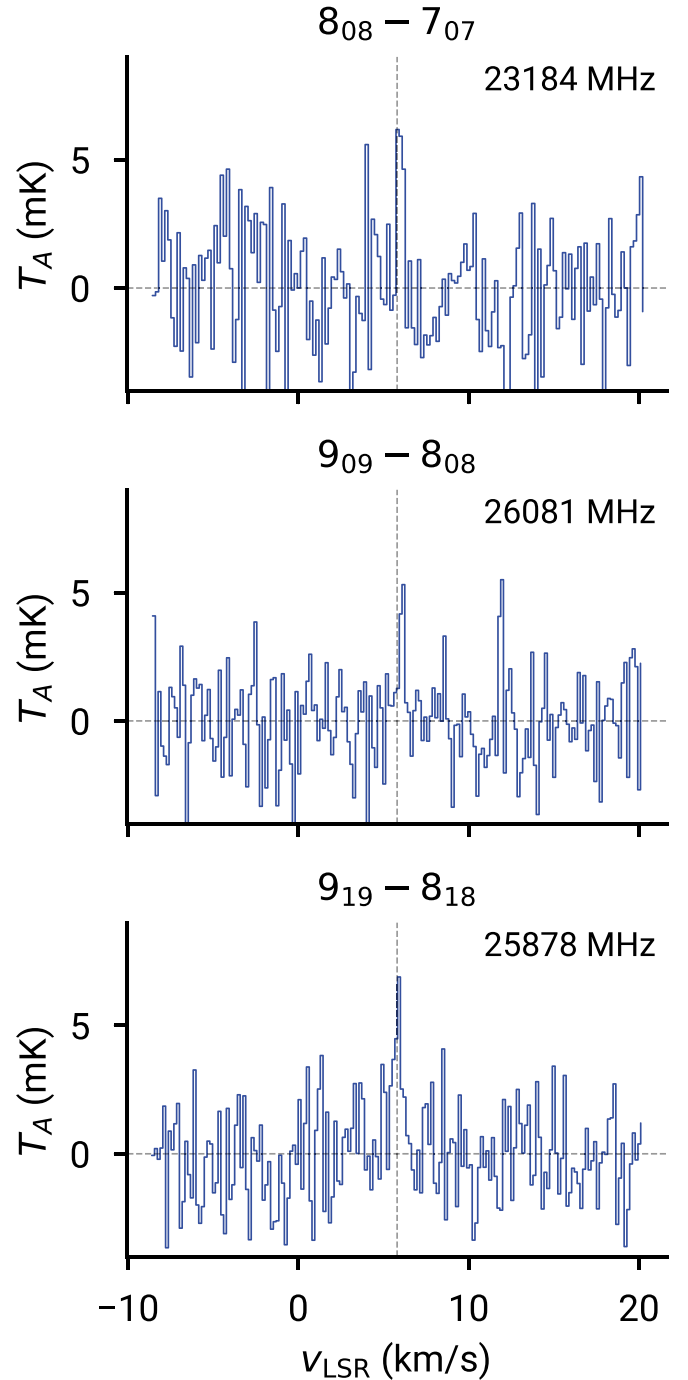

Figure 2. Observed spectral features in the GOTHAM spectrum (rebinned to 14 kHz resolution) at the center frequencies for three *a*-type transitions of *trans*-(E)-CVA. The dashed vertical line indicates the nominal source velocity at 5.8 km s^{-1}. Asymmetric top ($J_{K_a K_c}$) quantum number assignments are given at the top of each trace, along with their rest frequencies. The peak signal-to-noise ratio for each spectrum is on the order of $\sim 3\sigma$.

velocity stacking and matched filter analysis with MCMC simulations to derive statistically robust molecular parameters for all three isomers. Figure 3 visualizes the detection of VCA and *trans*-(E)-CVA, and nondetection of *trans*-(Z)-CVA with the velocity stack and matched filter analyses.

The velocity stacks in Figure 3 indicate the presence of additive spectral intensity across the GOTHAM survey for VCA and *trans*-(E)-CVA, and none for *trans*-(Z)-CVA. For
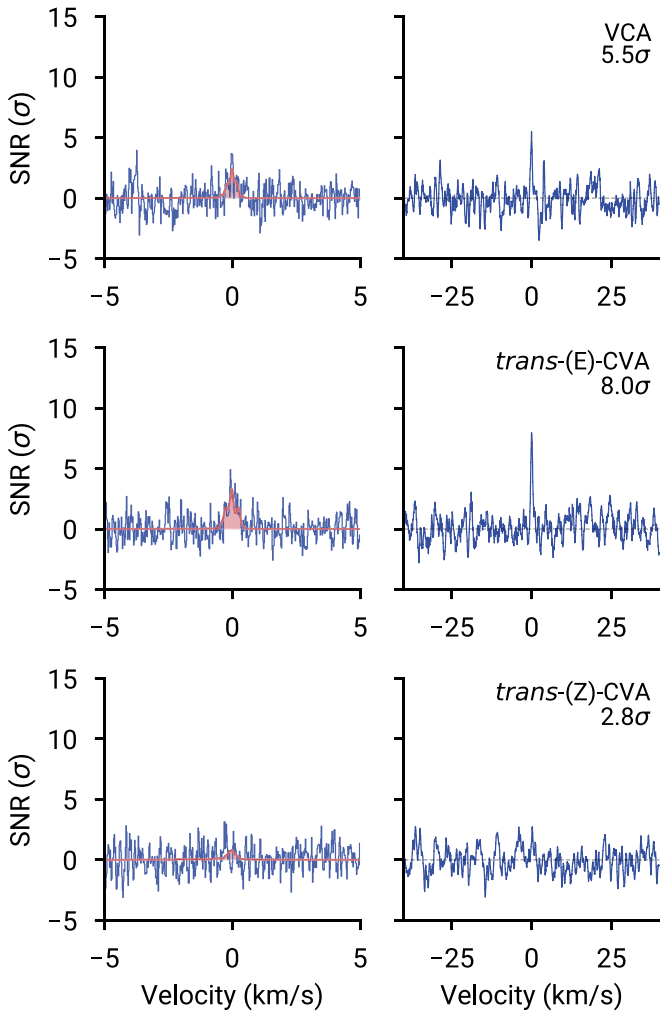
Figure 3. Velocity stack (left columns) and corresponding matched filter (right columns) for the three molecules of interest. Peak impulse responses—shown in units of signal-to-noise (S/N)—are provided in the matched filter plots. The velocity stack of simulated spectra using parameters derived from the MCMC simulations are overlaid in red.

Table 2
Total Column Densities and Excitation Temperatures Derived from the MCMC Simulations

Molecule	Column Density $(10^{11} \, cm^{-2})$	T_{ex} (K)
VCA[a]	$1.87^{+0.37}_{-0.38}$	$6.7^{+0.6}_{-0.6}$
trans-(E)-CVA[b]	$2.90^{+0.41}_{-0.40}$	$7.0^{+1.2}_{-1.3}$
trans-(Z)-CVA[c]	<2[d]	…

Notes. Uncertainties are given as the 95% credible interval. Unabridged MCMC results can be found in the Appendix. Interlopers refer to interfering features of other species, detected as 3σ for a given spectral chunk.
[a] Based on 271 transitions, with zero ignored due to interlopers.
[b] Based on 270 transitions, with one ignored due to interlopers.
[c] Based on 1354 transitions, with zero ignored due to interlopers.
[d] Upper limit given as the 97.5th percentile.

~7 K—consistent with those reported for other molecules in TMC-1 (Dobashi et al. 2018, 2019). The velocity profiles are also similar between each isomer, allowing us to assume that they are cospatial within each velocity component. Of the two isomers we successfully detected, VCA is approximately two times less abundant than trans-(E)-CVA, despite being more thermodynamically stable (~240 K), thus their relative abundance is dominated by kinetics. The third isomer, trans-(Z)-CVA, does not exhibit a significant response in either the velocity stack or the matched filter (Figure 3). However, our MCMC simulations indicate that it may be just below our current sensitivity limits (see Appendix A2).

Given that the relative abundances are likely dictated by kinetics, the question now turns to how the three isomers may be preferentially formed in TMC-1. In the gas phase, neutral–neutral reactions are an attractive route: radicals such as C_2H and CN can react with $CH_2 = CHC \equiv N$ (vinyl cyanide) and $CH_2 = CHC \equiv CH$ (vinyl acetylene), followed by hydrogen loss. The reaction $C_2H + CH_2 = CHC \equiv N$ and would produce stereoisomers of CVA, with a preference for the trans isomers due to steric hindrance owing to the acetylenic unit. While this specific reaction has not yet been studied experimentally, by analogy to similar reactions between C_2H and unsaturated hydrocarbons [C_2H_2 (Chastaing et al. 1998; Zhang et al. 2009; Kovács et al. 2010); C_2H_4, C_3H_6 (Chastaing et al. 1998; Krishtal et al. 2009; Bouwman et al. 2012)] we expect this reaction to be barrierless and efficient even at low temperatures. The latter reaction, $CN + CH_2 = CHC \equiv CH$, can form all three [$H_3C_5N$] isomers considered in Figure 1; experimental studies by Yang et al. (1992) and Sims et al. (1993) suggests CN addition is just as efficient to either the vinyl (forming CVA) or acetylenic unit (forming VCA) (Balucani et al. 2000; Choi et al. 2004). Additionally, VCA can be formed through the reaction between $C_3N + C_2H_4$ involving submerged barriers (Moon & Kim 2017); experimental kinetic data for this reaction is not yet available to the best of our knowledge.

Alternatively, grain surface reactions are a well-established pathway to hydrogenate unsaturated species efficiently (Herbst 2001; Cuppen et al. 2017). In this context, [H_3C_5N] molecules would be formed through $HC_5N + H_2$ hydrogenation, with the isomeric ratio dependent on the relative cross-section or likelihood of attaching H_2 to each respective part of the chain, which in turn is dictated by whether this occurs in a concerted ($+H_2$) or stepwise ($+H + H$) fashion. The former is likely to be highly endothermic and therefore unlikely under cold, dark conditions,
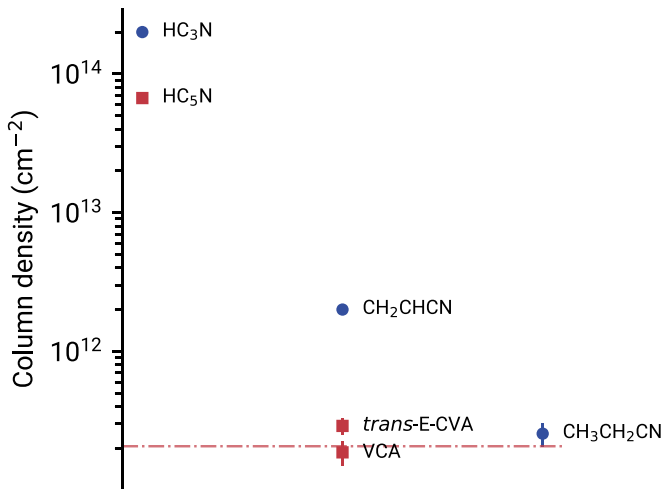
each stack, the red traces show the velocity stack for simulated spectra based on the posterior means from the MCMC simulations, which in all cases agrees well with the stacks based on observations. The two velocity stacks corroborate in the matched filter, simultaneously visualizing the overlap between model and observations, and providing an estimate of the significance of our detection. For VCA and trans-(E)-CVA, the matched filters exhibit a response clearly above the noise, whereas for trans-(Z)-CVA this is not the case and thus we report only an upper limit to the column density for this molecule. Table 2 summarizes the derived column densities and excitation temperatures from the MCMC simulations.

4.4. Astrochemical Implications

Based on our systematic investigation of the three lowest energy isomers of [H_3C_5N], we can infer some details into the relative importance of dynamical pathways that lead to the overall chemical inventory of TMC-1—particularly the branched unsaturated hydrocarbons we see here. In all cases, the excitation temperatures we estimate are on the order of

Figure 4. Column densities for assumed cospatial HC_3N and HC_5N (Loomis et al. 2020), CH_2CHCN (Matthews & Sears 1983), CH_3CH_2CN (Appendix A.4), and the newly detected molecules toward TMC-1. The error bars represent 1σ uncertainty.

while the latter is facilitated by hydrogen atom tunneling. A similar route had been proposed for CH_2CHCN, with HC_3N as the precursor (Blake et al. 1987). Analysis by Loomis et al. (2020) suggests HC_5N is approximately an order of magnitude less abundant than HC_3N, which corresponds well with isomers of the $[H_3C_5N]$ family and CH_2CHCN, where the column density of the latter was determined by Matthews & Sears (1983) to be on the order of $3 \times 10^{12}\,cm^{-2}$. An argument against hydrogenation reactions, however, is that prior to sublimation from the grain they should ultimately form saturated species that are known to be uncommon in TMC-1: for instance, ethyl cyanide (CH_3CH_2CN) should form from hydrogenation of CH_2CHCN (Blake et al. 1987). Minh & Irvine (1991) were only able to place upper limits on CH_3CH_2CN; using the same velocity stack and matched filter methodology, we tentatively ascribe an upper limit to the total column density of $<4 \times 10^{11}\,cm^{-2}$ (given as the 97.5th percentile; see Appendix A.4), consistent with their determination ($<3 \times 10^{12}\,cm^{-2}$).

While it is difficult to draw conclusions with confidence at this level of significance, it appears that the decrement in column density follows a qualitative trend (Figure 4) that lends credit to sequential hydrogenation ($HC_3N \xrightarrow{+H_2} CH_2CHCN \xrightarrow{+H_2} CH_3CH_2CN$). Better constraints on CH_3CH_2CN, as well as the missing isomer trans-(Z)-CVA will provide critical insight into the relative importance of gas phase and grain hydrogenation pathways.

If the hydrogenation route is indeed a large contributing mechanism, then VCA and trans-(E)-CVA would be important intermediates toward the formation of cyclic molecules—specifically the still-elusive N-heterocycles such as pyrrole and pyridine, and the recently detected 1-cyanocyclopentadiene. In the former, we note that trans-(Z)-CVA is a hydrogenation ($+H_2$) and ring closing step from pyridine—a molecule of biological importance. Further study into this isomeric family, particularly cis-CVA and the deuterated isotopologues (similar to previous work on cyanopolyyne isotopologues by Burkhardt et al. 2018), should reveal the dynamical processes behind the formation of these molecules, although their laboratory spectra have not yet been measured.

5. Conclusions

From our GOTHAM observations, we report the first detection of two new isomers of $[H_3C_5N]$ toward TMC-1, and more generally in the interstellar medium. Combining MCMC simulations with velocity stacking and matched filter analysis, we were able to successfully characterize vinylcyanoacetylene (VCA) and trans-(E)-cyanovinylacetylene (CVA) at 5.5σ and 8.0σ significance, respectively, with derived column densities on the order of 2×10^{11} and $3 \times 10^{11}\,cm^{-2}$ respectively. The third isomer, trans-(Z)-CVA, appears to be just out of reach at current integration levels, and from our MCMC analysis we place an upper limit for its column density at $<2 \times 10^{11}\,cm^{-2}$. While it remains unclear how these unsaturated hydrocarbons may be formed in TMC-1, we discuss implications of cyanopolyyne hydrogenation on grain surfaces—as part of this analysis, we also report a tentative detection of ethyl cyanide with an MCMC derived upper limit to the total column density of $<4 \times 10^{11}\,cm^{-2}$. Further analysis into the $[H_3C_5N]$ family, and other related hydrocarbon chains will help reveal the complex formation processes taking place, and more broadly, how molecules more saturated than cyanopolyynes could be formed under cold, dark conditions.

6. Data Access and Code

Data used for the MCMC analysis can be found in the DataVerse entry (GOTHAM 2020). The code used to perform the analysis is part of the MOLSIM open-source package; an archival version of the code can be accessed at Lee & McGuire (2020).

Appendix
MCMC Posterior Analysis

A.1. trans-(E)-CVA

Figure A1 shows the results of the MCMC fit for trans-(E)-CVA. There are several factors that warrant extra discussion, particularly as to how these plots can be interpreted. First, the diagonal traces correspond to the marginalized likelihood for each model parameter presented as empirical cumulative distribution function (ECDF) plots—these provide a nonparametric visualization of the likelihood, in contrast to kernel density estimates and histograms, which require length scale and bin width specification, respectively. Second, the
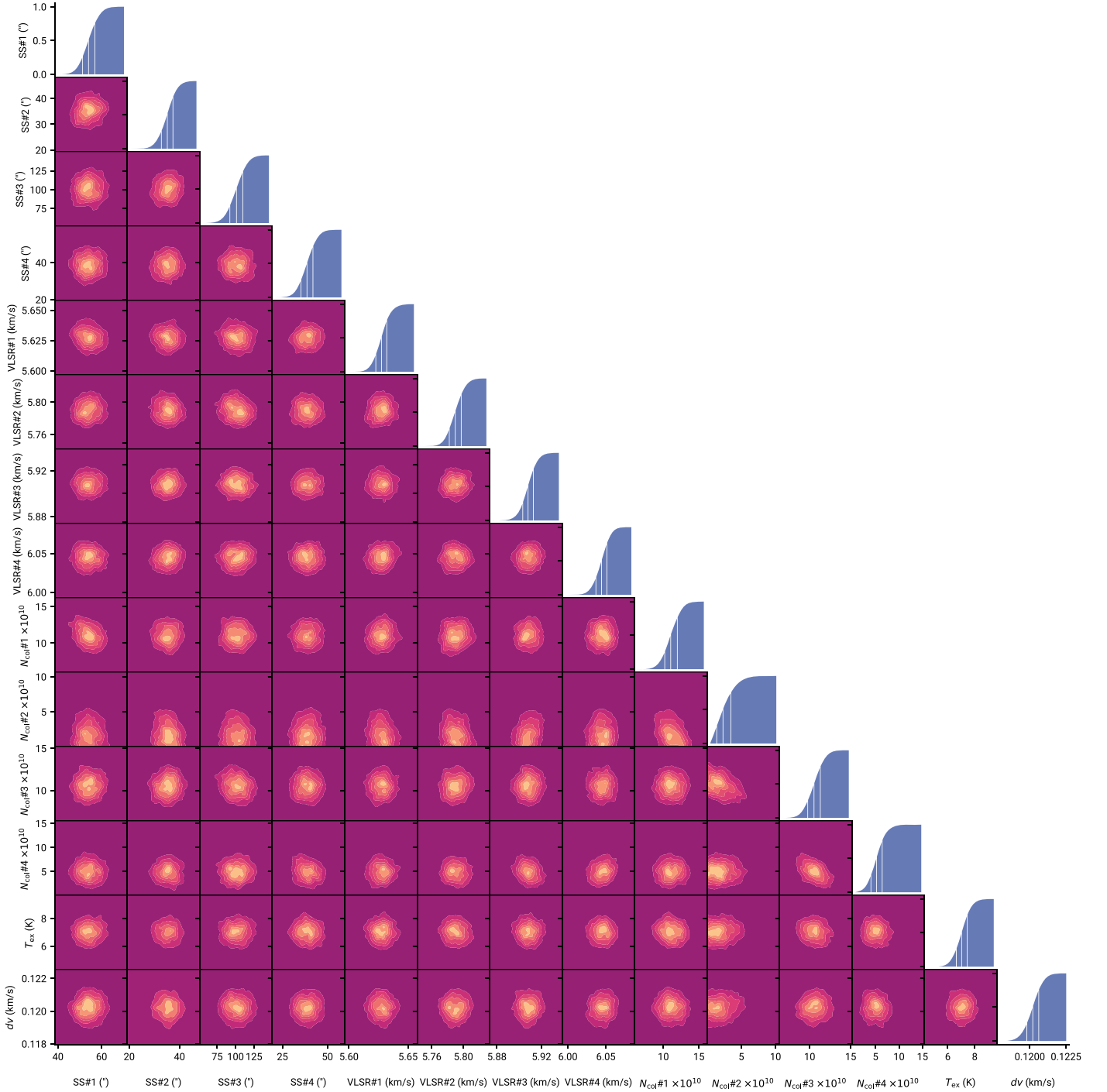
Figure A1. Corner plot for *trans*-(E)-CVA. The diagonal traces correspond to ECDF plots, and off-diagonal plots show the kernel density covariance between model parameters. In the former, lines represent the 25th, 50th, and 75th percentiles respectively. The length scale for the kernel density plots is chosen with Scott's rule.

off-diagonal traces correspond to kernel density plots of parameter pairs—these plots visualize the covariance between any given pair of model parameters; in our case, well-approximated by two-dimensional Gaussian distributions.

Inspection of the marginalized likelihood ECDF traces indicate firm detections in components #1, #3, and #4, with a likely nondetection in component number. In the nondetection case, the cumulative density rises linearly from zero N_{col}, while for detections they appear clearly sigmoid-like with the inflexion point at the nonzero column. Table A1 provides summary statistics for the posterior distributions.

A.2. trans-(Z)-CVA

Figure A2 shows the corner plot for *trans*-(Z)-CVA. Because these simulations fix the source size to the mean of *trans*-(E)-CVA, the source sizes are not sampled/fit and are omitted from the corner plot. Under these conditions, we observe the most likely nondetection in component #1, with evidence for detection in the remaining three components. Given that components #2 and #3 in particular are highly indicative of *trans*-(Z)-CVA, we believe that this molecule is just out of reach at the current level of integration of the second
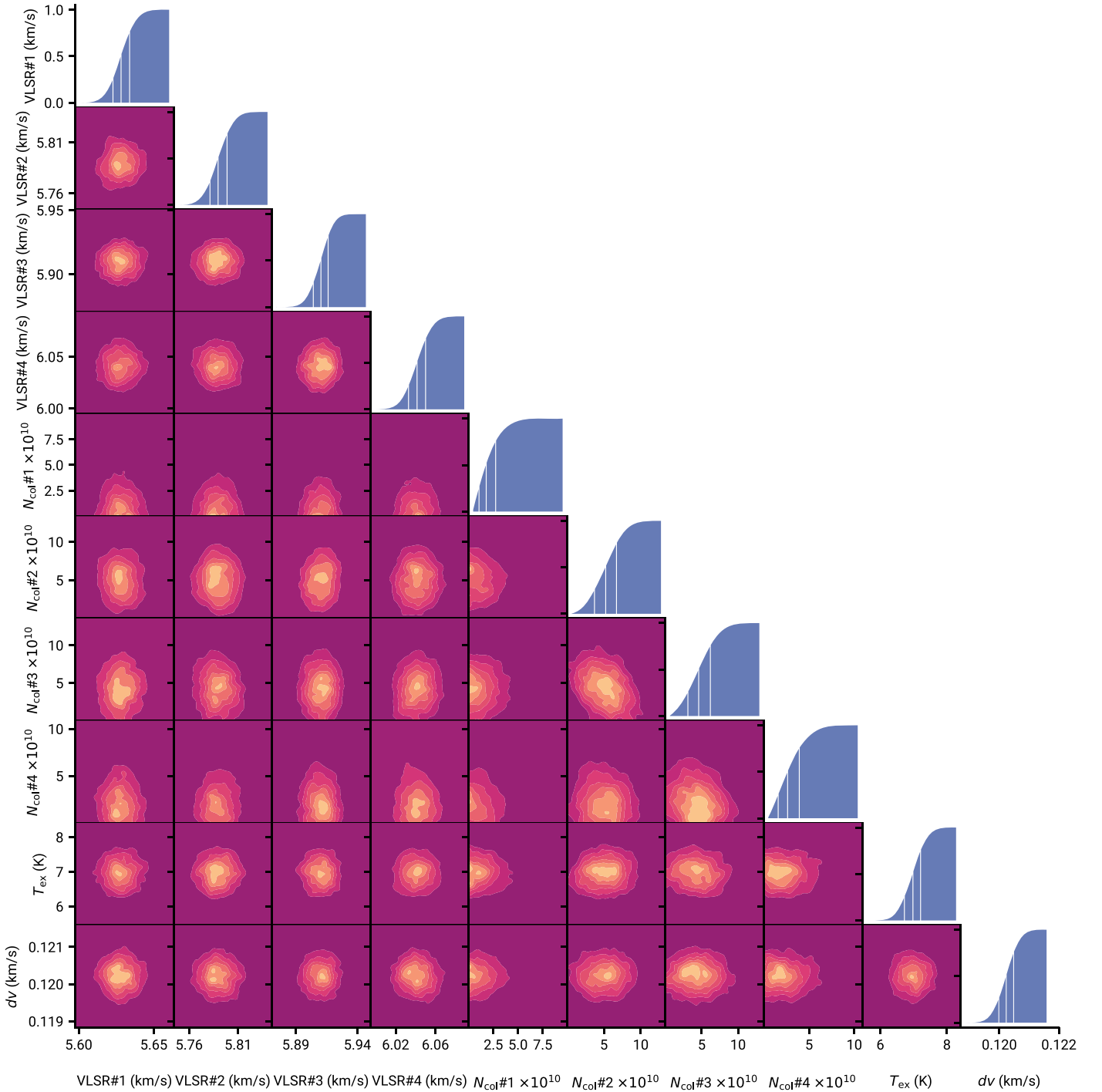
Figure A2. Corner plot for *trans*-(Z)-CVA. The diagonal traces correspond to ECDF plots, and off-diagonal plots show the kernel density covariance between model parameters. In the former, lines represent the 25th, 50th, and 75th percentiles respectively. The length scale for the kernel density plots is chosen with Scott's rule.

GOTHAM data release. Summaries of the posterior distributions can be found in Table A2.

A.3. VCA

Figure A3 visualizes the MCMC simulation results for VCA, with a similar treatment as to *trans*-(Z)-CVA. In contrast to the other molecules we have studied here, VCA demonstrates significant bimodality in its posterior distributions. Most of the observed flux can be explained by components #1 and #4, while our model displays large covariance with component #3,

likely suggesting a three-component model where #2 and #3 are degenerate. Summaries of the posterior distributions can be found in Table A3.

A.4. Ethyl Cyanide

As part of our analysis into the hypothesis of cyanopolyyne hydrogenation of HC_5N leading to the formation of $[H_3C_5N]$ isomers, we performed the same velocity stacking and matched filter analysis for ethyl cyanide, the hydrogenation product of vinyl cyanide, which in turn could be formed from
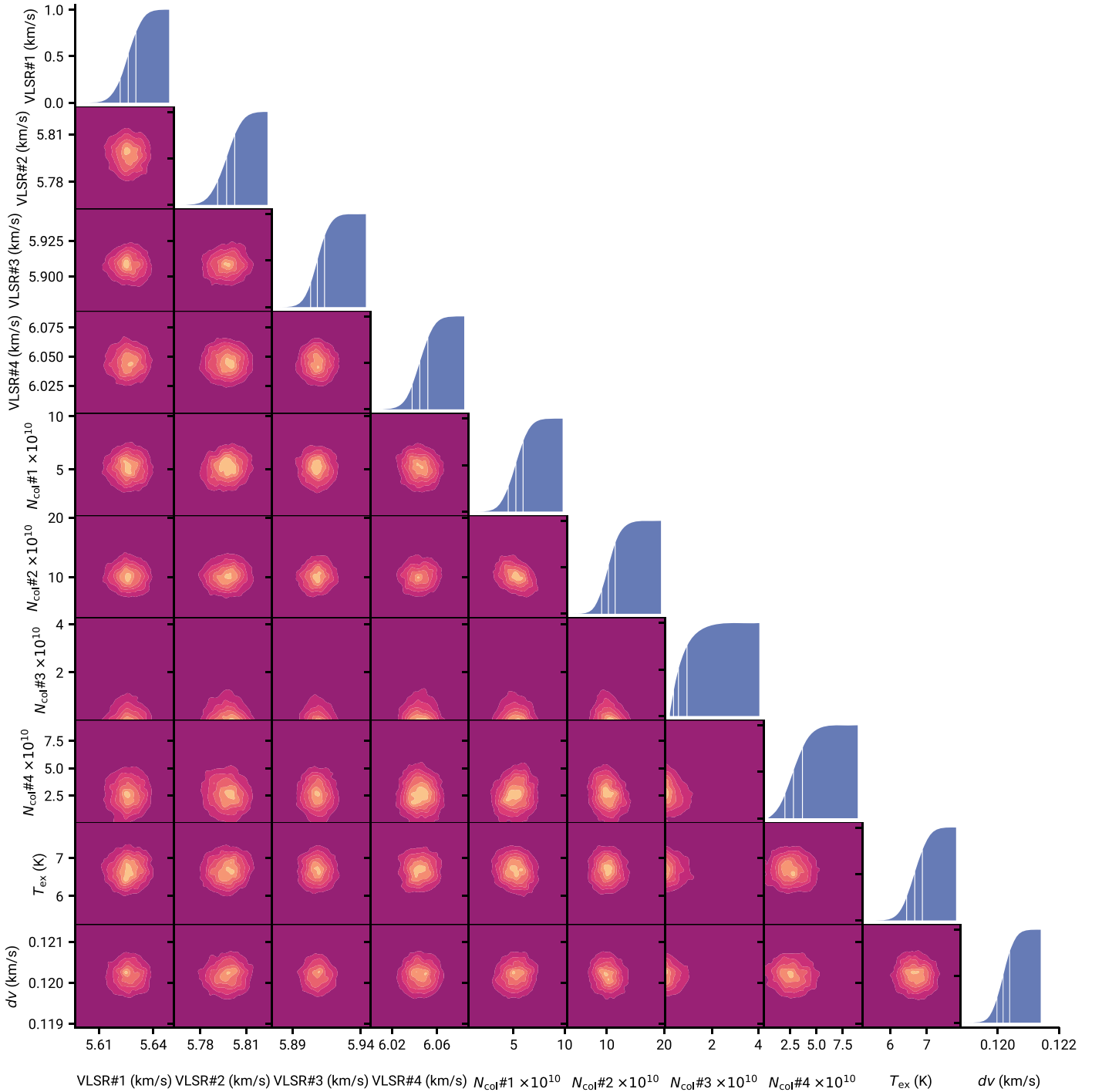
Figure A3. Corner plot for VCA. The diagonal traces correspond to ECDF plots, and off-diagonal plots show the kernel density covariance between model parameters. In the former, lines represent the 25th, 50th, and 75th percentiles, respectively. The length scale for the kernel density plots is chosen with Scott's rule.

hydrogenation of HC_3N. The catalog for ethyl cyanide was generated using spectroscopic parameters collated in the Cologne Database for Molecular Spectroscopy (Müller et al. 2005; Endres et al. 2016).

Individual transitions of ethyl cyanide were not observed at our current level of integration. Figure A4 shows the corner plot from the MCMC simulations, indicating likely detections toward components #1 and #2, and most likely nondetections in #3 and #4—a summary of the derived parameters can be found in Table A4. At our level of integration, it appears that there is supporting evidence for a tentative detection of ethyl cyanide, albeit at relatively low significance (Figure A5): as the quality of the GOTHAM spectrum improves, we can revisit this molecule in order to place better constraints on the model parameters, and correspondingly improve the matched filter response. At its current state, we establish an upper limit to the total column density based on the 97.5th percentile value from the joint posterior of $<4 \times 10^{11} \, cm^{-2}$.
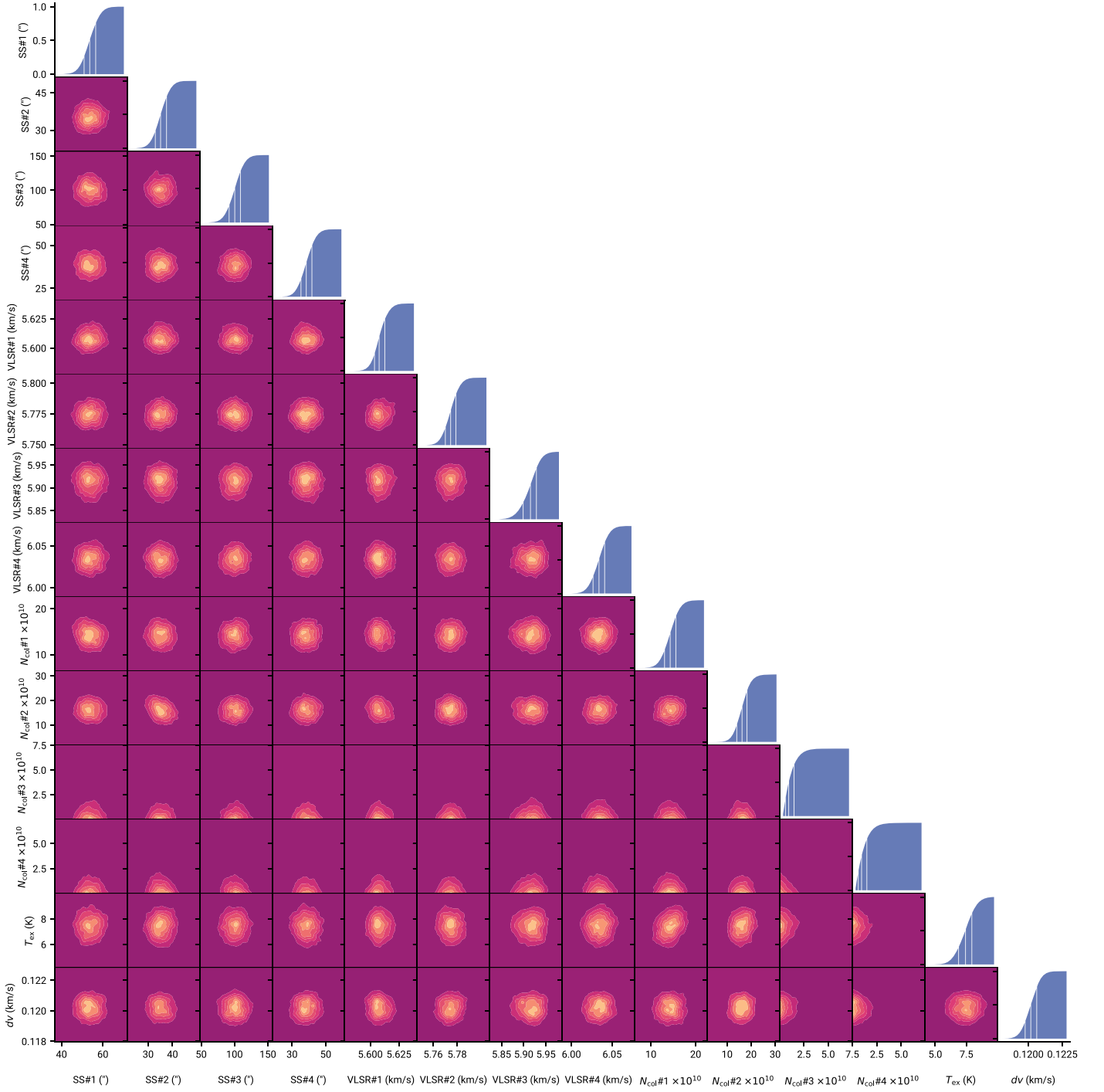
Figure A4. Corner plot for ethyl cyanide. The diagonal traces correspond to ECDF plots, and off-diagonal plots show the kernel density covariance between model parameters. In the former, lines represent the 25th, 50th, and 75th percentiles respectively. The length scale for the kernel density plots is chosen with Scott's rule.

Table A1
trans-(E)-CVA Best-fit Parameters from MCMC Analysis

Component	v_{lsr} (km s^{-1})	Size ($''$)	N_{col} (10^{10} cm^{-2})	T_{ex} (K)	ΔV (km s^{-1})
C1	$5.628^{+0.014}_{-0.015}$	54^{+8}_{-9}	$11.06^{+2.51}_{-2.59}$		
C2	$5.790^{+0.022}_{-0.021}$	35^{+7}_{-7}	$2.31^{+2.78}_{-2.31}$	$7.0^{+1.2}_{-1.3}$	$0.120^{+0.001}_{-0.001}$
C3	$5.908^{+0.015}_{-0.015}$	101^{+26}_{-25}	$10.52^{+2.27}_{-2.17}$		
C4	$6.044^{+0.021}_{-0.021}$	39^{+10}_{-10}	$5.04^{+3.72}_{-3.52}$		
N_T (Total)	$28.98^{+4.13}_{-3.98} \times 10^{10}$ cm^{-2}				

Note. Quoted uncertainties correspond to the 95% highest posterior density. N_T (Total) refers to the pooled column density from the four components, given as the posterior mean and 95% highest posterior density of the joint distributions.

Table A2
trans-(Z)-CVA Best-fit Parameters from MCMC Analysis

Component	v_{lsr} (km s^{-1})	N_{col} (10^{10} cm^{-2})	T_{ex} (K)	ΔV (km s^{-1})
C1	$5.628^{+0.017}_{-0.016}$	$1.72^{+2.45}_{-1.72}$		
C2	$5.789^{+0.025}_{-0.026}$	$5.07^{+4.15}_{-4.11}$		
C3	$5.910^{+0.017}_{-0.018}$	$4.47^{+3.77}_{-4.46}$	$7.0^{+0.7}_{-0.7}$	$0.120^{+0.001}_{-0.001}$
C4	$6.041^{+0.025}_{-0.025}$	$2.64^{+3.13}_{-2.64}$		
N_T (Total)	$13.96^{+6.40}_{-5.32} \times 10^{10}$ cm^{-2}			

Note. Quoted uncertainties correspond to the 95% highest posterior density. N_T (total) refers to the pooled column density from the four components, given as the mean and 95% highest posterior density of the joint posterior distributions.

Table A3
VCA Best-fit Parameters from MCMC Analysis

Component	v_{lsr} (km s^{-1})	N_{col} (10^{10} cm^{-2})	T_{ex} (K)	ΔV (km s^{-1})
C1	$5.626^{+0.013}_{-0.013}$	$5.185^{+2.183}_{-2.189}$		
C2	$5.797^{+0.017}_{-0.017}$	$10.218^{+3.526}_{-3.560}$		
C3	$5.908^{+0.016}_{-0.015}$	$0.569^{+1.002}_{-0.569}$	$6.7^{+0.6}_{-0.6}$	$0.124^{+0.003}_{-0.003}$
C4	$6.045^{+0.020}_{-0.021}$	$2.708^{+2.284}_{-2.474}$		
N_T (Total)	$18.669^{+3.704}_{-3.767} \times 10^{10}$ cm^{-2}			

Note. Quoted uncertainties correspond to the 95% highest posterior density. N_T (Total) refers to the pooled column density from the four components, given as the mean and 95% highest posterior density of the joint posterior distributions.

Table A4
Ethyl Cyanide Best-fit Parameters from MCMC Analysis

Component	v_{lsr} (km s^{-1})	Size ($''$)	N_{col} (10^{10} cm^{-2})	T_{ex} (K)	ΔV (km s^{-1})
C1	$5.608^{+0.014}_{-0.013}$	54^{+9}_{-8}	$14.29^{+3.80}_{-3.73}$		
C2	$5.760^{+0.018}_{-0.018}$	35^{+7}_{-7}	$16.19^{+6.40}_{-6.33}$		
C3	$5.914^{+0.042}_{-0.047}$	100^{+25}_{-25}	$0.86^{+1.38}_{-0.86}$	$7.4^{+1.5}_{-1.7}$	$0.120^{+0.001}_{-0.001}$
C4	$6.034^{+0.021}_{-0.021}$	38^{+9}_{-10}	$0.88^{+1.38}_{-0.88}$		
N_T (Total)	$32.05^{+4.07}_{-4.00} \times 10^{10}$ cm^{-2}				

Note. Quoted uncertainties correspond to the 95% highest posterior density. N_T (total) refers to the pooled column density from the four components, given as the mean and 95% highest posterior density of the joint posterior distributions.
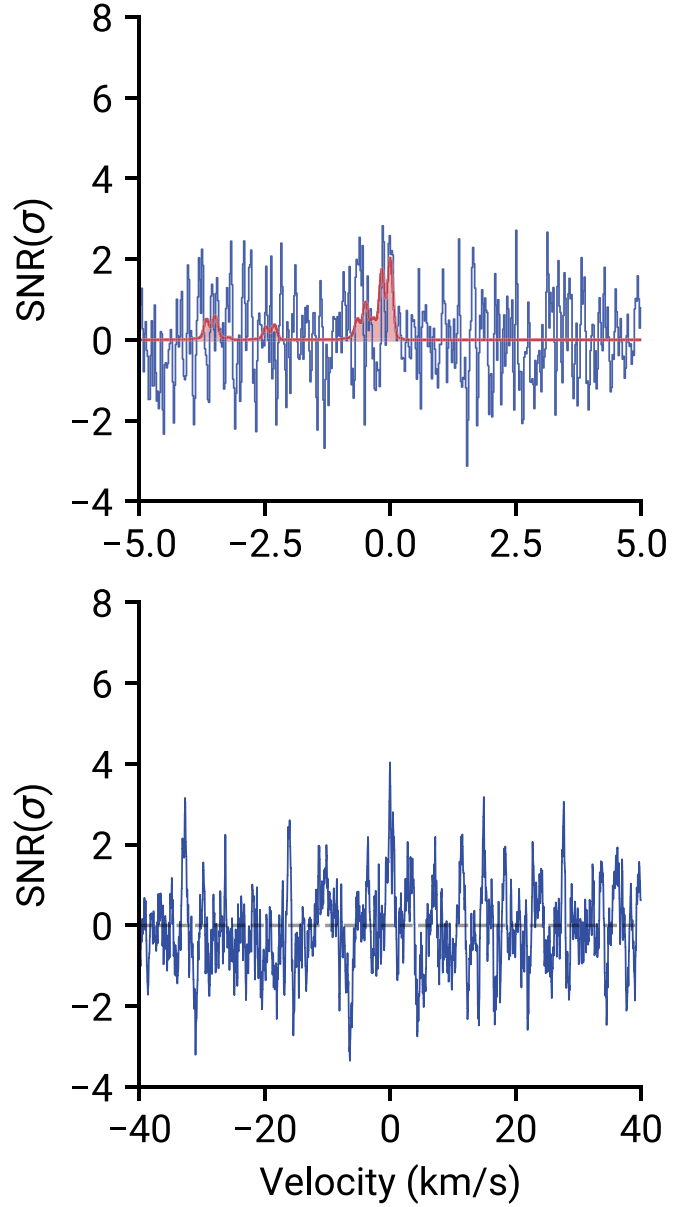

Figure A5. Velocity stack and matched filter plots for ethyl cyanide. The peak matched filter response is 4.17σ.

ORCID iDs

Kin Long Kelvin Lee ⓘ https://orcid.org/0000-0002-1903-9242
Ryan A. Loomis ⓘ https://orcid.org/0000-0002-8932-1219
Andrew M. Burkhardt ⓘ https://orcid.org/0000-0003-0799-0927
Ilsa R. Cooke ⓘ https://orcid.org/0000-0002-0850-7426
Ci Xue ⓘ https://orcid.org/0000-0003-2760-2119
Mark A. Siebert ⓘ https://orcid.org/0000-0002-8505-4934
Christopher N. Shingledecker ⓘ https://orcid.org/0000-0002-5171-7568
Anthony Remijan ⓘ https://orcid.org/0000-0001-9479-9287
Michael C. McCarthy ⓘ https://orcid.org/0000-0001-9142-0008
Brett A. McGuire ⓘ https://orcid.org/0000-0003-1254-4817

References

Baboul, A. G., Curtiss, L. A., Redfern, P. C., & Raghavachari, K. 1999, JChPh, 110, 7650
Balucani, N., Asvany, O., Huang, L. C. L., et al. 2000, ApJ, 545, 892

Blake, G. A., Sutton, E. C., Masson, C. R., & Phillips, T. G. 1987, ApJ, 315, 621

Bouwman, J., Goulay, F., Leone, S. R., & Wilson, K. R. 2012, JPCA, 116, 3907

Brünken, S., Gupta, H., Gottlieb, C. A., McCarthy, M. C., & Thaddeus, P. 2007, ApJL, 664, L43

Burkhardt, A. M., Herbst, E., Kalenskii, S. V., et al. 2018, MNRAS, 474, 5068

Burkhardt, A. M., Loomis, R. A., Shingledecker, C. N., et al. 2021, NatAs, in press

Chastaing, D., James, P. L., Sims, I. R., & Smith, I. W. M. 1998, FaDi, 109, 165

Choi, N., Blitz, M. A., McKee, K., Pilling, M. J., & Seakins, P. W. 2004, CPL, 384, 68

Cuppen, H. M., Walsh, C., & Lamberts, T. 2017, SSRv, 212, 1

Dobashi, K., Shimoikura, T., Nakamura, F., et al. 2018, ApJ, 864, 82

Dobashi, K., Shimoikura, T., Ochiai, T., et al. 2019, ApJ, 879, 88

Endres, C. P., Schlemmer, S., Schilke, P., Stutzki, J., & Müller, H. S. P. 2016, JMoSp, 327, 95

Foreman-Mackey, D., Hogg, D. W., Lang, D., & Goodman, J. 2013, PASP, 125, 306

Frisch, M. J., Trucks, G. W., Schlegel, H. B., et al. 2016, Gaussian 16 Revision A.01

Gelman, A., & Rubin, D. B. 1992, Bayesian Statistics (Oxford: Oxford Univ. Press), 625

GOTHAM 2020, Spectral Stacking Data for Phase 2 Science Release of GOTHAM, V2, Harvard Dataverse, doi:10.7910/DVN/K9HRCK

Halter, R. J., Fimmen, R. J., McMahon, R. L., et al. 2001, JAChS, 123, 12353

Herbst, E. 2001, Chemical Society Reviews, 30, 168

Kovács, T., Blitz, M. A., & Seakins, P. W. 2010, JPCA, 114, 4735

Krishtal, S. P., Mebel, A. M., & Kaiser, R. I. 2009, JPCA, 113, 11112

Kumar, R., Carroll, C., Hartikainen, A., & Martin, O. 2019, JOSS, 4, 1143

Langer, W. D., Velusamy, T., Kuiper, T. B. H., et al. 1997, ApJL, 480, L63

Lee, K. L. K., & McGuire, M. 2020, JPCA, 5, 898

Lee, K. L. K., & McGuire, B. A. 2020, Molsim, Zenodo, https://zenodo.org/record/4122749

Loomis, R. A., Burkhardt, A. M., Shingledecker, C. N., et al. 2020, arXiv:2009.11900

Loomis, R. A., Öberg, K. I., Andrews, S. M., et al. 2018, AJ, 155, 182

Matthews, H. E., & Sears, T. J. 1983, ApJ, 272, 149

McCarthy, M. C., Lee, K. L. K., Carroll, P. B., et al. 2020a, JPCA, 124, 5170

McCarthy, M. C., Lee, K. L. K., Loomis, R. A., et al. 2020b, NatAs, in press

McGuire, B. A., Burkhardt, A. M., Kalenskii, S., et al. 2018, Sci, 359, 202

McGuire, B. A., Burkhardt, A. M., Loomis, R. A., et al. 2020a, ApJL, 900, L10

McGuire, B. A., Loomis, R. A., Burkhardt, A. M., et al. 2020b, Sci, in press

Minh, Y. C., & Irvine, W. M. 1991, Ap&SS, 175, 165

Moon, J., & Kim, J. 2017, Theoretical Chemistry Accounts, 136, 13

Müller, H. S. P., Schlöder, F., Stutzki, J., & Winnewisser, G. 2005, JMoSt, 742, 215

Pickett, H. M. 1991, JMoSp, 148, 371

Simmie, J. M., & Somers, K. P. 2015, JPCA, 119, 7235

Sims, I. R., Queffelec, J.-L., Travers, D., et al. 1993, CPL, 211, 461

Soma, T., Sakai, N., Watanabe, Y., & Yamamoto, S. 2018, ApJ, 854, 116

Thaddeus, P., Gottlieb, C. A., Hjalmarson, A., et al. 1985, ApJL, 294, L49

Thorwirth, S., McCarthy, M. C., Dudek, J. B., & Thaddeus, P. 2004, JMoSp, 225, 93

Vigren, E., Hamberg, M., Zhaunerchyk, V., et al. 2009, ApJ, 695, 317

Xue, C., Willis, E. R., Loomis, R. A., et al. 2020, ApJL, 900, L9

Yang, D. L., Yu, T., Wang, N. S., & Lin, M. C. 1992, CP, 160, 317

Zhang, F., Kim, Y. S., Kaiser, R. I., Krishtal, S. P., & Mebel, A. M. 2009, JPCA, 113, 11167